



HAL
open science

Stress accumulation in the Marmara Sea estimated through ground-motion simulations from dynamic rupture scenarios

Hideo Aochi, John Douglas, Thomas Ulrich

► **To cite this version:**

Hideo Aochi, John Douglas, Thomas Ulrich. Stress accumulation in the Marmara Sea estimated through ground-motion simulations from dynamic rupture scenarios. *Journal of Geophysical Research : Solid Earth*, 2017, 10.1002/2016JB013790 . hal-01849904

HAL Id: hal-01849904

<https://brgm.hal.science/hal-01849904>

Submitted on 23 Jun 2023

HAL is a multi-disciplinary open access archive for the deposit and dissemination of scientific research documents, whether they are published or not. The documents may come from teaching and research institutions in France or abroad, or from public or private research centers.

L'archive ouverte pluridisciplinaire **HAL**, est destinée au dépôt et à la diffusion de documents scientifiques de niveau recherche, publiés ou non, émanant des établissements d'enseignement et de recherche français ou étrangers, des laboratoires publics ou privés.

RESEARCH ARTICLE

10.1002/2016JB013790

Key Points:

- Earthquake ground motions are simulated in the Marmara Sea region based on dynamic rupture scenarios
- Ground motion prediction equations (GMPEs) allow the revision of the probabilities of model parameters used in a logic tree framework
- The revised probabilities thereby support the hypothesis of the low-stress conditions for this part of the North Anatolian Fault

Supporting Information:

- Figure S1

Correspondence to:

H. Aochi,
aochi.hideo@gmail.com

Citation:

Aochi, H., J. Douglas, and T. Ulrich (2017), Stress accumulation in the Marmara Sea estimated through ground-motion simulations from dynamic rupture scenarios, *J. Geophys. Res. Solid Earth*, 122, 2219–2235, doi:10.1002/2016JB013790.

Received 29 NOV 2016

Accepted 22 FEB 2017

Accepted article online 27 FEB 2017

Published online 22 MAR 2017

Stress accumulation in the Marmara Sea estimated through ground-motion simulations from dynamic rupture scenarios

Hideo Aochi¹ , John Douglas² , and Thomas Ulrich³

¹Bureau de Recherches Géologiques et Minières, Orléans, France, ²Department of Civil and Environmental Engineering, University of Strathclyde, Glasgow, UK, ³Department of Earth and Environmental Sciences, Ludwig-Maximilians-Universität, München, Germany

Abstract We compare ground motions simulated from dynamic rupture scenarios, for the seismic gap along the North Anatolian Fault under the Marmara Sea (Turkey), to estimates from empirical ground motion prediction equations (GMPEs). Ground motions are simulated using a finite difference method and a 3-D model of the local crustal structure. They are analyzed at more than a thousand locations in terms of horizontal peak ground velocity. Characteristics of probable earthquake scenarios are strongly dependent on the hypothesized level of accumulated stress, in terms of a normalized stress parameter T . With respect to the GMPEs, it is found that simulations for many scenarios systematically overestimate the ground motions at all distances. Simulations for only some scenarios, corresponding to moderate stress accumulation, match the estimates from the GMPEs. The difference between the simulations and the GMPEs is used to quantify the relative probabilities of each scenario and, therefore, to revise the probability of the stress field. A magnitude M_w7+ operating at moderate prestress field ($0.6 < T \leq 0.7$) is statistically more probable, as previously assumed in the logic tree of probabilistic assessment of rupture scenarios. This approach of revising the mechanical hypothesis by means of comparison to an empirical statistical model (e.g., a GMPE) is useful not only for practical seismic hazard assessments but also to understand crustal dynamics.

1. Introduction

The part of the North Anatolian Fault under the Marmara Sea (Turkey) is recognized as a major seismic gap, where a large earthquake of magnitude larger than 7 is expected in the coming years [Atakan *et al.*, 2002; Erdik *et al.*, 2004; Parsons, 2004]. Seismic risk mitigation plans have been developed around this gap, in particular, for the megacity of Istanbul, in terms of, for example, early warning systems using dense observation networks and structural retrofitting. Regardless of the high seismic hazard/risk, the description of the potential source area remains imprecise, principally because the faults are running under the Marmara Sea, the largest earthquakes were not recorded instrumentally as they occurred in the eighteenth century or earlier [e.g., Ergintav *et al.*, 2014, and references therein], and the current seismicity rate is relatively low. Many studies have been carried out to assess potential earthquake scenarios in this area [e.g., Erdik *et al.*, 2004; Pulido *et al.*, 2004; Oglesby *et al.*, 2008; Oglesby and Mai, 2012]. Among them, Aochi and Ulrich [2015, hereafter referred as AU15], have discussed statistically the occurrence probability of various earthquake scenarios, which are dynamically simulated along different nonplanar fault systems for various levels of hypothesized stress accumulation and hypocentral locations. Although each model parameter is assigned a probability, this process is based on expert judgment through a logic tree approach. It is found that some scenarios correspond to extreme conditions, such as a very fast rupture velocity (supershear rupture), which leads to high-amplitude ground motions [e.g., Akinci *et al.*, 2016]. The purpose of this article is to quantify the ground-motion variations as a function of the hypotheses, especially with respect to stress accumulation, through comparisons with empirical ground motion prediction equations (GMPEs) [e.g., Douglas, 2003], which are simple models used extensively in engineering seismology to estimate ground motions at a site given the occurrence of an earthquake of a particular magnitude and location.

There have been several attempts to validate numerical simulations of earthquake ground motions using GMPEs (e.g., Southern California Earthquake Center broadband platform validation exercise [Goulet *et al.*, 2015]), which had been previously derived from curve fitting to observations. Aochi and Douglas [2006] compare ground motions that were dynamically simulated from simple earthquake scenarios (double-couple

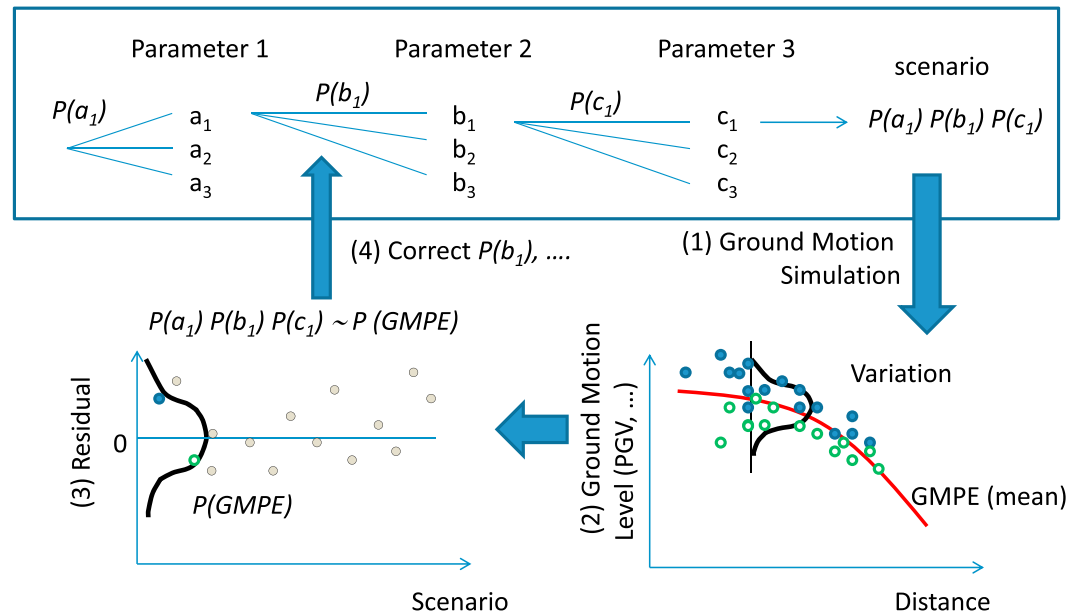


Figure 1. Schematic illustration of forward modeling of earthquake scenarios and inversion process to calibrate the model parameters initially given. (top) Simulation steps in a logic tree with three branch levels (parameters 1, 2, and 3). Each set of choices of model parameters has a probability $P(a_1)P(a_2)P(a_3)$, such that the simulation results can be discussed statistically as demonstrated in AU15. (bottom) (1) Each earthquake scenario leads to a ground-motion simulation. (2) The ground motion of different scenarios (different color circles) can be compared with GMPE (red curve as mean with a lognormal distribution). (3) Position of simulated ground motions within a lognormal distribution of GMPE is calculated for each scenario. (4) This derivative may infer the likelihood of each scenario so as to revise the probabilities of model parameters of interest.

sources) to GMPEs for various intensity measures: peak ground acceleration (PGA), peak ground velocity (PGV), response spectral acceleration, Arias intensity, and duration. Although there were no complex propagation or site effects in the simulations, the results implied a strong dispersion of the ground motion due only to source effects. *Baumann and Dalguer [2014]* show more systematically the consistency of ground-motion simulations from dynamic rupture modeling with GMPEs for frequencies up to 1 Hz, in particular, for intermediate distances (between 10 and 45 km). They also observed supersaturation (a large variation both in positive and negative senses) very close (less than 1 km) to the source. Although most of the studies are for planar faults, ground motion from dynamic rupture simulations based on nonplanar fault systems can also be coherent in terms of different metrics such as PGV, duration, and response spectral ordinates [*Aochi and Yoshimi, 2016*].

In the following sections, we first explain the procedure of our analysis, in which model parameters are “inverted” from the difference between the ground motion simulated for different dynamic rupture scenarios and those predicted by GMPEs. Then we introduce the simulations both in terms of the earthquake source and the 3-D regional structure, such that the calculated ground motions are comparable with available observations for this region. Finally, we discuss the implications of our analysis for this area and more generally for future seismic hazard assessments.

2. Method and Model

In this section we present the method followed in this article and the models used to make the calculations.

2.1. Method

Figure 1 illustrates schematically the forward modeling of earthquake scenarios and ground-motion simulations in a logic tree formulation (top) and an inversion with respect to the GMPE for calibrating the model-parameter probabilities (bottom), from steps (1) to (4). Each forward modeling is a deterministic process based on fracture mechanics and elastodynamics under given conditions. Various model parameters are considered together with a weighting probability based on expert judgment, as in many recent probabilistic seismic hazard assessments [e.g., *Douglas et al., 2014*]. In the forward modeling of AU15, three variable model parameters are considered, and for each of which three branches are given, namely, $3 \times 3 \times 3 = 27$, simulations

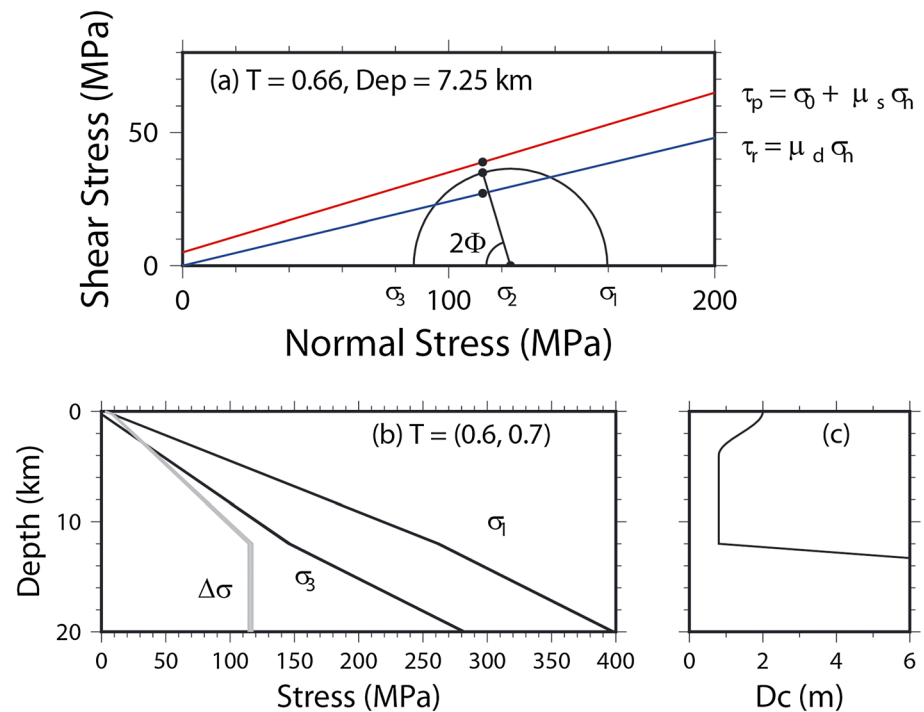


Figure 2. Model parameters used in AU15. (a) A Mohr-Coulomb diagram for the case of $T=0.66$ and 7.25 km depth. Stress parameter T constrains the position of Mohr circle, defined by principal stresses σ_1, σ_2 , and σ_3 , between static and dynamic friction lines defined by σ_0, μ_s , and μ_d . The optimal direction of σ_1 is set to 36.7° from the tectonic rotation of the Marmara block. (b) Maximum and minimum principal stress (σ_1 and σ_3) ranges for $T=(0.6, 0.7)$ as a function of depth (the curves for the two values of T overlap, but their variations are small). $\Delta\sigma = \sigma_1 - \sigma_3$ is also shown. Initial normal and shear stress on each portion of the fault system is given in a function of $\Delta\sigma$. (c) Assumed variation of D_c with depth of a linear slip-weakening friction. In the shallow crust and below 12 km depth, a relatively stable frictional regime is assumed. More details are given in AU15.

are carried out, with probabilities between 0.5% and 7.5%. The model parameters are (1) fault geometry, (2) stress accumulation level, and (3) hypocentral location. This study focuses only on the variation in stress accumulation level, which strongly affects the simulated ground motions. Previously, the three increasing levels of stress accumulation were attributed decreasing probabilities, i.e., higher probability for a lower stress accumulation. This assumption is reasonable in the sense that a characteristic earthquake may be triggered once the regional accumulated stress is just sufficient, without requiring a high and unstable stress. The assigned probabilities, however, remain uncertain. We previously remarked that some simulated scenarios show severe or extreme features, such as very large slip velocity and/or very fast rupture propagation (i.e., supershear rupture) and, thus, lead to extreme ground motions (AU15). Such scenarios are most commonly associated to a high accumulated stress and are given a low probability. However, they appear quite frequently so that, in the sum, they become statistically important. The motivation of this study is to quantify the resultant ground motions so as to better constrain the probabilities of different stress accumulation levels.

For convenience, we briefly explain the stress conditions and friction that are essential in dynamic rupture simulations. AU15 introduced a stress parameter T indicating the closeness of a given Mohr circle to Coulomb friction stick threshold in a Mohr-Coulomb diagram (Figure 2). Parameter T is a global, nondimensional parameter that describes the externally loaded principal stresses, namely, the initial level of stress loading and the frictional parameters, and is uniform everywhere in a simulation. The condition of $T=1$ means that the Mohr circle tangentially meets the static friction threshold τ_p :

$$\tau_p = \sigma_0 + \mu_s \cdot \sigma_n, \tag{1}$$

where σ_0 is the cohesive force, μ_s is the static frictional coefficient, and σ_n is the applied normal stress. Following simulations of the 1999 Izmit earthquake [Aochi and Madariaga, 2003], these parameters are set as $\sigma_0 = 5$ MPa and $\mu_s = 0.3$. Mapping the regional stress tensor on the complex fault leads to spatially heterogeneous shear and normal stress acting on the fault. In the simulations, the external principal stress direction

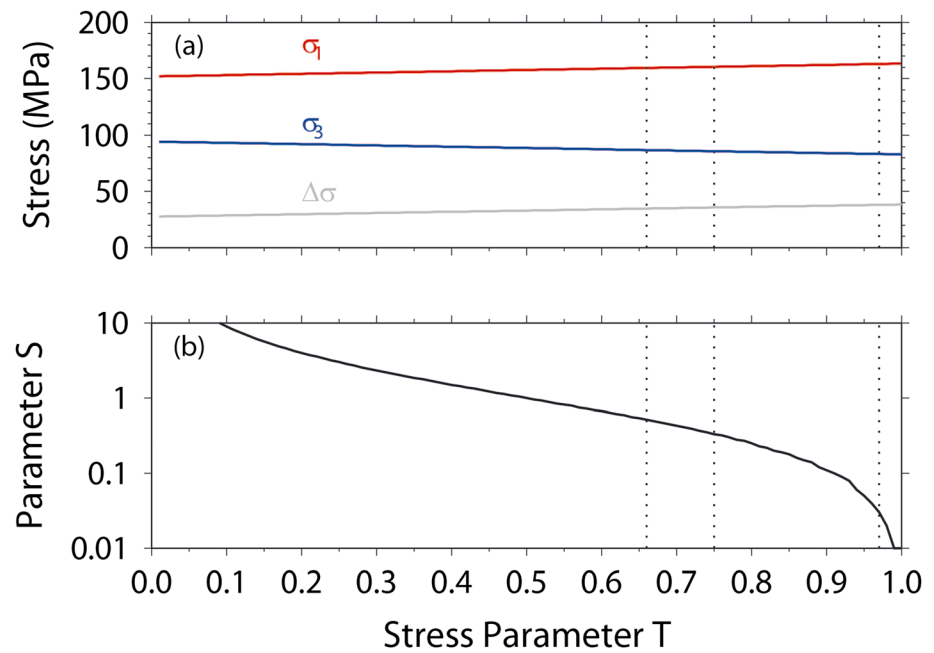


Figure 3. (a) Variations of σ_1 , σ_3 , and $\Delta\sigma$ as a function of stress parameter T . (b) Relation between parameter S of Das and Aki [1977] and stress parameter T . S here is calculated for the optimal fault orientation with respect to the external principal stresses. In the simulations, S varies along the fault strike in each simulation. The vertical dotted lines correspond to the three different levels of T studied in AU15 ($T = 0.66, 0.75, \text{ and } 0.97$).

is set according to the tectonic movement [Le Pichon et al., 2003], and its absolute level varies with depth. The condition of $T = 0$ means, in contrast, that the Mohr circle tangentially meets the dynamic friction threshold τ_r :

$$\tau_r = \mu_d \cdot \sigma_n, \tag{2}$$

where the dynamic frictional coefficient μ_d is set equal to 0.24, 20% less than μ_s , which allows modeling the released fracture energy during the earthquake [e.g., McGarr, 1999] (thus, always $\tau_p > \tau_r$). T is given by

$$T \equiv \frac{\tau_0 - \tau_r}{\tau_p - \tau_r} \text{ for an optimal fault orientation } (\Phi = 36.7^\circ; \text{ see Figure 2}). \tag{3}$$

We assume that the seismogenic zone extends down to 12 km depth and that its shallow part is less favorable to rupture propagation. As a consequence, we introduce a depth-dependent critical displacement (D_c of the slip-weakening law; Figure 2c), identical to the depth-dependent D_c used by Aochi and Madariaga [2003] to simulate the 1999 Izmit earthquake. For a positive stress drop during an earthquake, T must be between 0 and 1. If a planar fault is ideally oriented with respect to the external principal stress, the condition $T = 0.5$ easily allows spontaneous rupture propagation (this corresponds to $S = 2$ of Das and Aki [1977]); however, this is not the case for a nonplanar fault system. Figure 3 shows the principal stresses as a function of stress parameter. Although the rupture process is sensitive to the parameter T (or S), the external principal stress does not change significantly. Note that S is only defined for a planar fault, while stress parameter T is defined in a Mohr-Coulomb diagram such that stress conditions can be calculated for faults of any orientation. It should also be noted that S is strongly variable along the fault traces for a given T . In this study, we vary T when discussing in detail the probability distribution.

The purpose of this study is to constrain the probable stress levels by analyzing statistically the calculated ground motions of various scenarios by comparing them to estimates from GMPEs (final step of Figure 1). GMPEs are generally obtained by regression analysis on intensity measures, such as PGA and PGV, computed from observed strong motion data. GMPEs are usually simple functions of earthquake magnitude, faulting mechanism, source-to-site distance, and local site conditions. The equations provide a median value as well as its associated standard deviation. Therefore, the deviation of the simulated ground motions with respect to the GMPEs indicates a likelihood of each case, and the degree of this deviation can be used to update the probabilities of model parameters of interest among the bins.

Scherbaum *et al.* [2009] and Delavaud *et al.* [2012] propose and demonstrate the model selection of GMPEs using an information-theoretic approach. For every sampling point $(x_i, i = 1, \dots, N)$, function $g(x)$ evaluates the likelihood of observing x (ground-motion estimate) for a given reference model (GMPE, here). Negative average sample log likelihood (LLH) is therefore defined as

$$\text{LLH}(g) = -\frac{1}{N} \sum_{i=1}^N \log_2(g(x_i)), \quad (4)$$

which is a good estimate of the relative distance between a model and a given reference. A small LLH means a close match between the model and the observation. Then, for residuals from different models $g_k(x)$, $k = 1, \dots, K$, the likely weight of each model p_j is given as

$$p_j = \frac{2^{-\text{LLH}(g_j)}}{\sum_{k=1}^K 2^{-\text{LLH}(g_k)}}. \quad (5)$$

This criterion provides a simple expression to rank the models statistically. Hence, this can be regarded as a probabilistic inversion process. Equation (5) provides a relative probability among all the bins, which is used in logic tree (Figure 1). The bins may be biased for some reasons, but the probability provided by equation (5) is valid in the framework of a logic tree.

In this study, we calculate the ground motions in the 3-D structure using a finite difference method [Aochi and Madariaga, 2003; Aochi *et al.*, 2013] according to different finite source scenarios dynamically simulated. For the purpose mentioned above, we adopt PGV as the primary intensity measure as we find that our tests on moderate earthquakes (M of about 5) show a consistency among the simulation, the observations, and the GMPEs (section 2.3) and also because PGV is sensible at lower frequencies (around 1 Hz), which we calculate than PGA. Below we also demonstrate that other metrics lead to similar findings.

2.2. Models

Various earthquake scenarios along the North Anatolian Fault under the Marmara Sea were dynamically simulated using the 3-D boundary integral equation method (AU15). Each of the 27 simulated scenarios has a probability between 0.5 and 7.5% and results in earthquakes with moment magnitudes (M_w) between 5.49 and 7.56. Each scenario is given a weight corresponding to the selected model parameters for fault geometry, stress accumulation level, and hypocentral location in a logic tree formulation as explained in the previous section. The assigned probabilities remain, however, qualitative and uncertain, in particular, for the stress accumulation level, which significantly controls the consequent ground motions. Figure 4 presents three examples of dynamic rupture simulations based on three different stress levels ($T = 0.66, 0.75$, and 0.97) along the same fault geometry and assuming the same hypocenter (AU15). After forcing rupture on an initial crack in the same way, the subsequent dynamic rupture propagation is controlled by energy balance due to the static and dynamic stress field and a frictional law. The external principal stress determined by parameter T is assumed homogeneous along the tectonic rotational movement of the Marmara block, but the applied normal/shear stress field along the fault trace is heterogeneous with respect to the strike direction. Irregularity in fault geometry perturbs the stress field. If the assumed accumulated stress (T) is high enough, the rupture propagation overcomes the stress heterogeneity to become a large earthquake. This tendency is what we generally observe in similar numerical simulations of dynamic rupture process along nonplanar faults such as the 1999 Izmit earthquake nearby, for example [Harris *et al.*, 2002; Aochi and Madariaga, 2003]. As a result, the ruptured area, the amount of slip, and the magnitude of an earthquake, hence, become larger ($M_w 7.04, 7.27$, and 7.46) as T increases (Figure 4), and these changes should influence the ground motions (AU15).

The ground-motion simulations are carried out in a 3-D structural model using a finite difference method, as in AU15. The finite difference is based on approximations that are fourth order in space and second order in time for a staggered grid scheme [Aochi and Madariaga, 2003; Aochi *et al.*, 2013, and references therein]. In the model domain of 200 km (EW) by 120 km (NS) by 40 km (UD), the 3-D structural model combines a 3-D tomographic model [Bayrakci *et al.*, 2013], bathymetry from the General Bathymetric Chart of the Ocean, and a 1-D layered model (H. Karabulut, personal communication, 2012; see Figure 5). The 3-D model describes the basin structure of the Marmara Sea, but it assumes a flat surface. The sea layer is given by

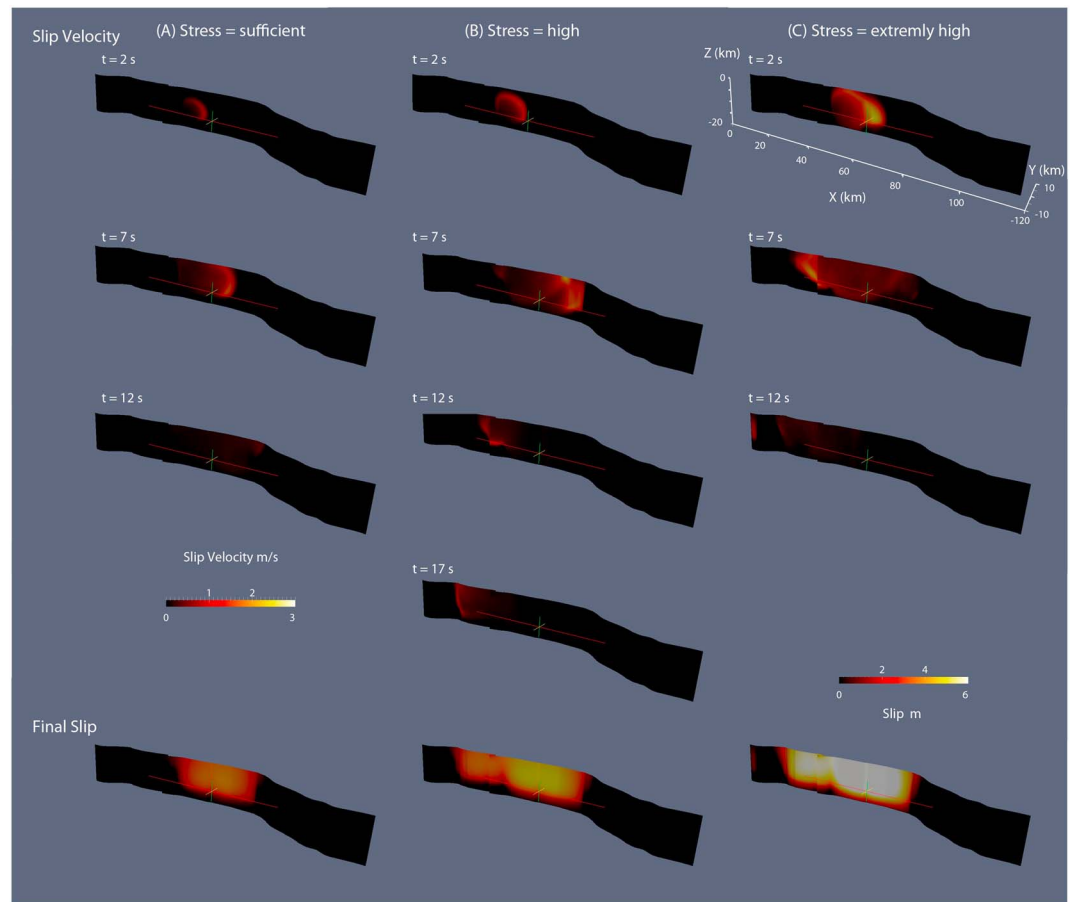


Figure 4. Snapshot of three representative dynamic rupture simulations along the North Anatolian Fault in the Marmara Sea (redrawn from AU15). Fault geometry and hypocenter locations are similar; only the stress conditions are different: (a) sufficient ($T=0.66$), (b) high ($T=0.75$), and (c) extremely high ($T=0.97$), controlled by one single-parameter T . The bottom row shows the final slip distribution. The resultant magnitudes M_w are 7.04, 7.27, and 7.46, respectively.

$V_p = 1.5$ km/s, $V_s = 0$ km/s, and $\rho = 1000$ kg/m³. The 3-D model of Bayrakci et al. [2013] gives only the structure of V_p , so we define V_s and the material density ρ simply by the following equations: $V_s = V_p/\sqrt{3}$ and $\rho = 1000 \times (-0.045 V_s^2 + 0.432 V_s + 1.711)$, where V_s is in km/s and ρ is in kg/m³ [Ludwig et al., 1970; Horikawa et al., 2008]. Figure 5 shows a 1-D profile extracted from the constructed 3-D model. The basin structure is pronounced down to about 12 km. The minimum velocity (V_{min}) included is about 0.8 km/s (V_s beneath the seafloor). We set the grid size of the finite difference scheme as $\Delta s = 160$ m. The maximum frequency f_{max} that is reliable numerically in the fourth-order approximation is estimated as $f_{max} = V_{min}/(5 \cdot \Delta s) = 1.0$ Hz. Our simulations do not take into account any site effects beyond those accounted for directly by the simulations. However, we can assume that at the relatively low frequencies considered, site effects may have minimal impact on the ground motions. The maximum velocity included in this model is $V_{max} = 7.94$ km/s (V_p). Therefore, a time step of the finite difference should be $\Delta t \leq 0.5 \cdot \Delta s/V_{max} = 0.010$ s to ensure stability, and, hence, we fix $\Delta t = 0.008$ s. Each calculation is run for a duration of 120 s. The quality factor Q for anelastic attenuation is introduced as a damping term in the finite difference formulation [Graves, 1996] with central frequency about 1 Hz. There are other methods to take Q into account in viscoelastic [e.g., Day and Bradley, 2001; Kristek and Moczo, 2003] or viscoplastic [e.g., Roten et al., 2014] formulations. However, as shown in the next section, our current knowledge of this region is still limited, even in terms of velocity structure, and a detailed description of attenuation would not be useful yet.

2.3. Current Model Performance

We first simulate a moderate earthquake to check the reliability of the 3-D model and the accuracy of the ground-motion simulations. Figure 6 shows the maps of the 25 July 2011 M_L 5.2 earthquake

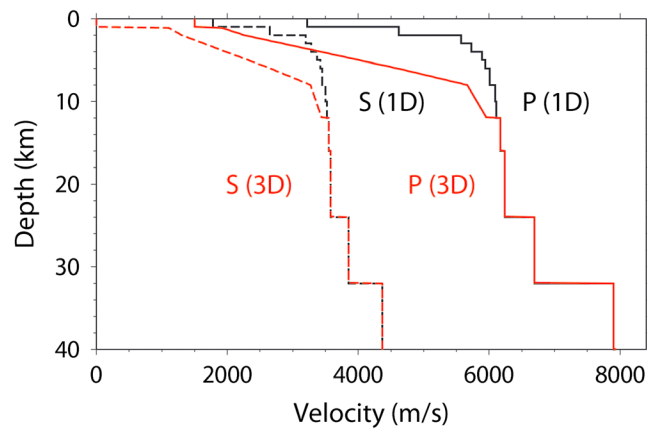


Figure 5. P and S wave velocity structures used in the simulations. The black lines represent the 1-D layered base model (Karabulut, personal communication, 2012). The red lines show a profile extracted from the constructed 3-D model based on the 3-D tomography results of Bayrakci et al. [2013] in the middle of the Marmara Sea, at the location of 7 June 2012 earthquake (see Figure 6).

(40.823°N, 27.743°E; 10.8 km depth) and the 7 June 2012 M_L 5.1 earthquake (40.853°N, 27.920°E; 7.1 km depth) (Karabulut, personal communication, 2012, who also provided their focal mechanisms) and available seismograph stations (broadband stations from Kandilli Observatory of Earthquake Research Institute, Turkey). For comparison, we calculate the ground motions using the 1-D layered model with a fixed $Q=300$ and the 3-D model assuming $Q=V_s/10$ (Figure 5). Moment magnitude M_w of 4.85 and 4.9 are given to obtain the best fit to the spectral accelerations at 20 s. The source time function is assumed as a spline function of durations of 2.0 s and 1.8 s, respectively.

Figure 7 shows the waveforms filtered up to 1 Hz at the common stations for the two earthquakes, aligned at the origin time ($t=0$). The arrivals of the waves are generally good except for SLVT, where the observed wave arrives slightly later than the simulated one. The peak values of the waveforms (here, PGV) are mostly caused by the direct S wave, but they are associated with the later phases at station SLVT. In our models, no 3-D structure exists beneath SLVT. This indicates that the model could be further improved locally to reflect the geological context. As well as considering a single ground-motion parameter, such as PGV, we also calculate the goodness of fit (GoF) score between simulations and observations based on several metrics from each time series [Olsen and Mayhew, 2010; Aochi and Yoshimi, 2016], averaged over long-period spectral acceleration (SA) (10, 20, and 50 s), short-period SA (1, 2, and 5 s), and duration defined as interval between 5 and 95% of Arias intensity. GoF for two positive values (x, y) to compare is calculated with

$$\text{GoF} = \text{erfc}\left(\frac{2|x-y|}{x+y}\right) \tag{6}$$

where erfc is the complementary error function. Figure 8 shows the scores averaged over the defined metrics for each component for the two earthquakes. We do not aim to discuss the scores of any particular station; we intend to show that the 3-D model is better than the 1-D layered model in this area. In general, GoF scores larger than 0.8 and 0.6 are considered “excellent” and “good,” respectively, so that the current 3-D model could be further improved. Note that a factor of 2 difference between values leads to $\text{GoF}=0.35$, although it would be better to compare spectra not by its linear amplitude but by its logarithm. Hereafter, we use the 3-D model assuming $Q=V_s/10$ for ground-motion simulations of large scenario earthquakes. Assumption of much stronger attenuation of $Q=V_s/20$ does not give a better result in terms of GoF, as the duration becomes very short.

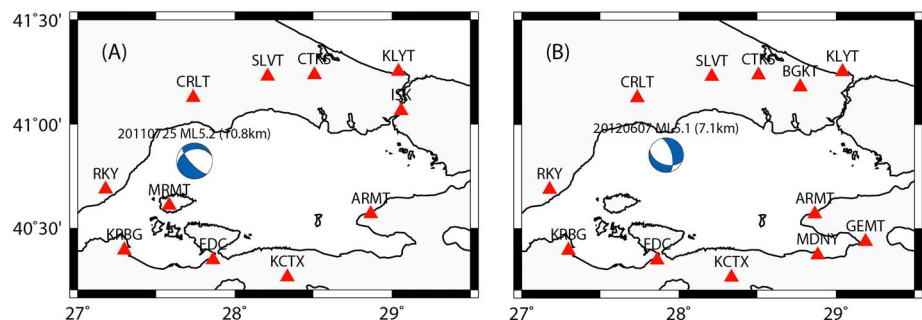


Figure 6. Maps of two moderate earthquakes and the available seismic stations from the broadband network of the Kandilli Observatory of Earthquake Research Institute. (a) M_L 5.2 25 July 2011 and (b) M_L 5.1 7 June 2011 earthquakes.

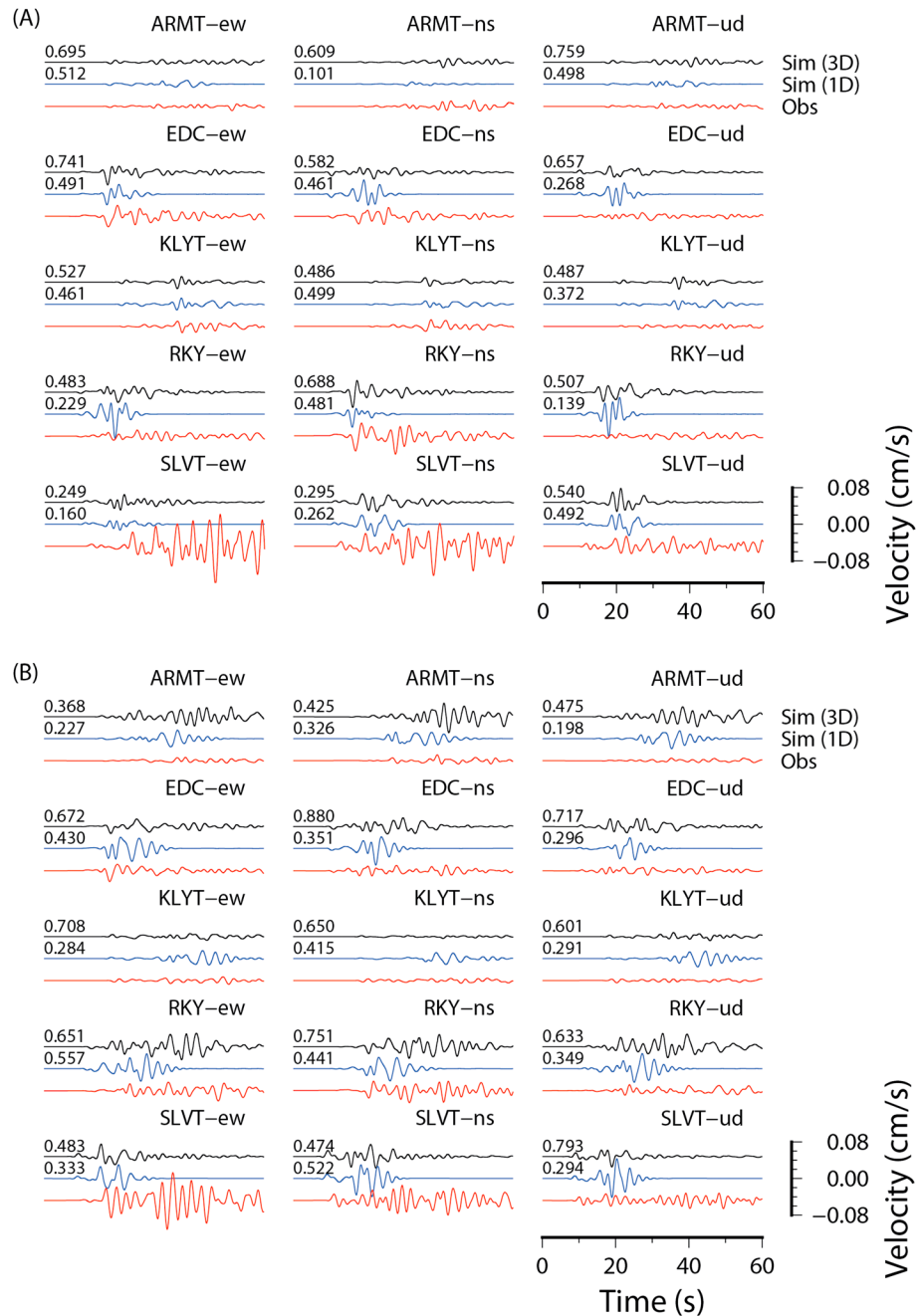


Figure 7. Comparison between simulated ground motions and observations at five common stations for (a) 25 July 2011 and (b) 7 June 2012 earthquakes. All the waveforms are filtered between 0.01 and 1 Hz. Two synthetics correspond to the simulations in a 3-D structure with $Q = V_s/10$ (black) and a 1-D layered model with fixed $Q = 300$, respectively.

We also compare the horizontal PGVs with GMPEs in Figure 9. The selected GMPEs are *Bindi et al.* [2014], *Akkar et al.* [2014a, 2014b], *Boore et al.* [2014], and *Cauzzi et al.* [2015]. We show the nonfiltered values of PGV from both simulations and observations because the duration of the source time function of a smooth B-spline function is given for 1 s in the simulations. The comparisons show a good coherency between the simulations and the observations for both the moderate earthquakes. Although the used source parameter is simple (a smooth source time function at a point source) in these tests, this agreement is supportive of applying any of these GMPEs at a frequency of around 1 Hz for large scenario earthquakes for which no observations exist. For the nearby 1999 Izmit earthquake, *Bouchon et al.* [2002] showed the near-field ground velocities with no filtering and used them directly for seismological analyses. The waveforms were dominated by low-frequency

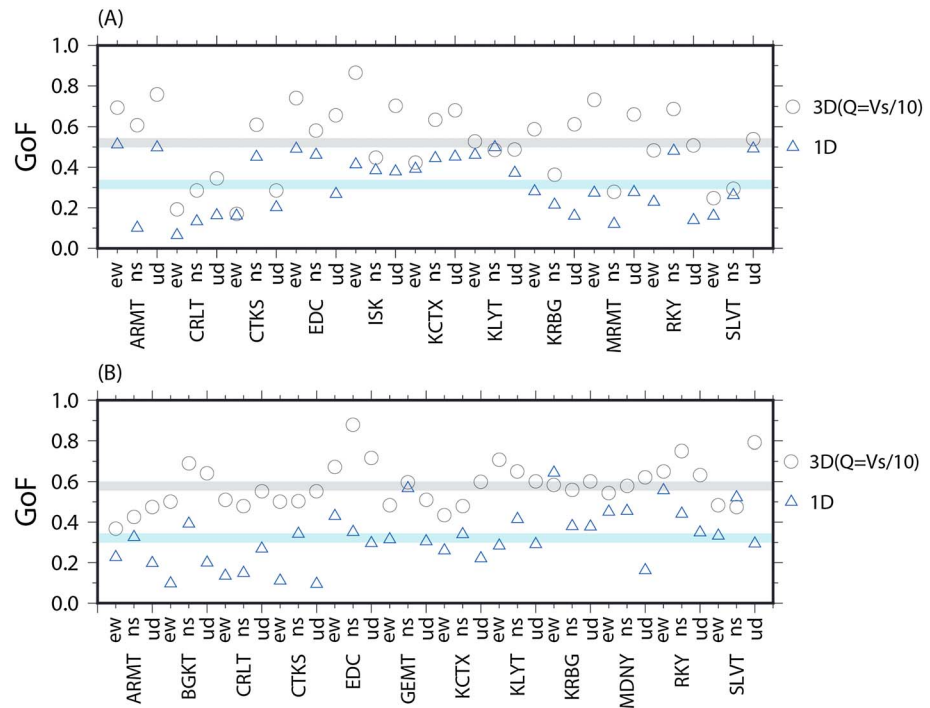


Figure 8. GoF scores between simulations and observations for (a) 25 July 2011 and (b) 7 June 2012 earthquakes (see also Figures 6 and 7). The scores are based on SA at various short and long periods and on duration metrics. We tested 1-D structure and 3-D structure assuming $Q = V_s/10$. The scores are calculated for each component at each station. The average over all the components and stations are shown by bold horizontal lines (3-D: black and 1-D: blue).

content: strong pulses of about a few seconds are visible and are closely related to the earthquake source process [e.g., *Aochi et al., 2011*]. In the following section, we use the GMPE of *Bindi et al.* [2014], which is found roughly in the middle of the considered GMPEs and the simulations and was found by *Douglas and Aochi* [2016] to be suitable for ground-motion simulations from moderate earthquakes in this region. Similar results would be found for any of the other three GMPEs as they predict similar ground motions.

3. Results

Let us first explore the PGV maps simulated for an $M_w 7.27$ earthquake scenario (central hypocenter position with $T = 0.75$; shown in Figure 4b). We calculate the ground motions assuming a constant $Q = 300$ or a

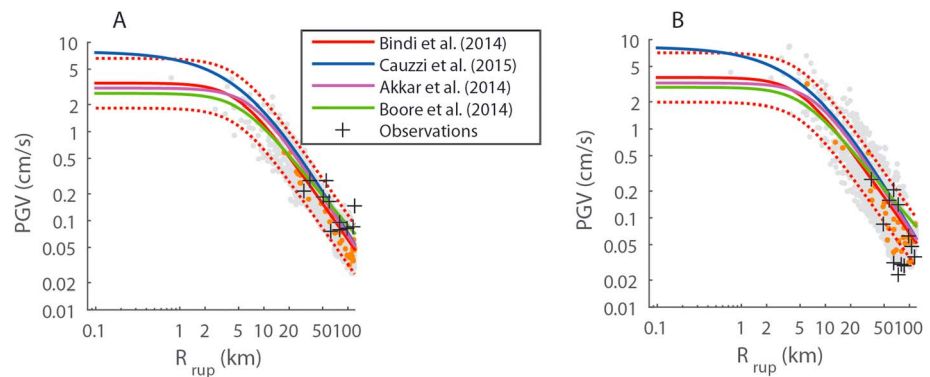


Figure 9. Comparison of the horizontal geometric-mean peak ground velocities (PGVs) for (a) the 25 July 2011 earthquake and (b) the 7 June 2012 earthquake. The gray points represent the simulations (3-D structure with $Q = V_s/10$) at the 2851 receivers distributed on the ground surface (about every 3 km). The red points show particularly the simulations at the receiver positions corresponding to the KOERI network, and the crosses are the observations available from the KOERI network for each earthquake. No filter is applied. Note that a duration of the source time function of 1 s is given in the simulations. Four GMPEs are compared, as listed in the legend. The standard deviation of *Bindi et al.*'s [2014] GMPE is shown by broken lines.

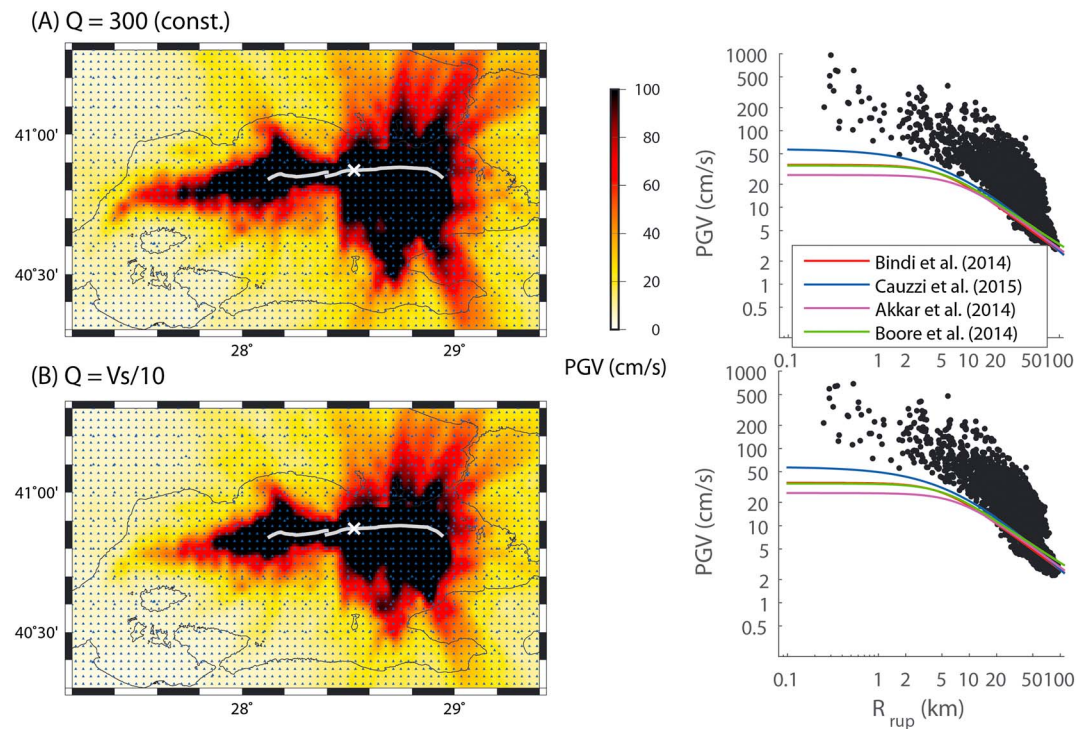


Figure 10. Comparison of the horizontal PGV map from the M_w 7.27 earthquake scenario shown in Figure 4b. The ground motions are calculated assuming (a) $Q = 300$ (constant) or (b) $Q = V_s/10$. The small triangles show the grid of receivers composed of 2851 points. The hypocenter position is shown by a cross and the ruptured fault portion by a bold white line. (right) The simulated PGVs are compared with those predicted by the empirical GMPEs of *Bindi et al.* [2014], *Cauzzi et al.* [2015], *Akkar et al.* [2014a, 2014b], and *Boore et al.* [2014]. The curve of *Bindi et al.* [2014] is overlapping almost perfectly that of *Boore et al.* [2014].

variable $Q = V_s/10$. Figure 10 shows the PGV maps and PGVs as a function of distance, evaluated at 2851 distributed receivers. Both the calculations tend to overestimate the ground-motion levels predicted by the GMPE of *Bindi et al.* [2014]. For comparison, the three other recent GMPEs considered above are also shown. Although some differences are found at distances shorter than 5 km, all these GMPEs show similar overall features. The simulated PGVs are high particularly in the near field compared with the predictions of GMPEs, but we find that strong attenuation ($Q = V_s/10$) shows a smaller average residual (in terms of common logarithms): 0.402 compared to 0.467. Hereafter, our discussion is based on the calculations assuming $Q = V_s/10$. Ground motions at very short distances of a few numerical grids of finite difference method should not be taken into account because each fault element of 500 m size within the boundary integral equation method simulation is represented as point source in the ground-motion simulations; namely, seismic moment release on a finite subelement of finite surface is concentrated at a point. The residuals are calculated for distances larger than 1 km. For farther distances, the receiver coverage is no longer azimuthally uniform as our physical model dimension is 200 km \times 120 km. Thus, we use distances up to 60 km, which is roughly the distance from the fault to the outer model boundary. We recall that the purpose of this study is not to adjust the model parameters to fit the GMPEs but to assess the probabilities of the model parameters using the relative discrepancy between the simulations and the GMPEs.

We keep the same fault geometry as in Figure 4 (model LP, based on the fault trace mapping of *Le Pichon et al.* [2003]) and the three hypocentral locations (west, center, and east; approximately at 28.2°E, 28.5°E, and 28.8°E, respectively). Since only six simulations, featuring three different stress levels, are available for $M_w \sim 7$ events from AU15 for the selected fault geometry, we carry out supplementary simulations for various stress levels. Figure 11 shows the simulated magnitudes of earthquakes with respect to the stress parameter T . It is found that the simulated magnitudes do not always depend linearly on T . Each increase in magnitude corresponds to the activation of a farther segment after a geometrical irregularity. It is also confirmed that the position of the hypocenter changes the possible progress of rupture propagation even under the same stress

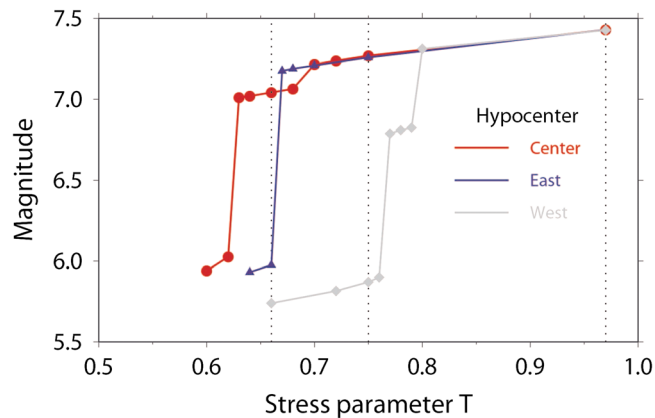


Figure 11. Simulated earthquake magnitudes as a function of the stress parameter T . We test the same three hypocentral positions as AU15. Previously, only the three levels ($T = 0.66, 0.75,$ and 0.97 , indicated as dotted lines) were simulated by AU15.

conditions, as inferred in previous studies [e.g., *Oglesby et al., 2008*]. Finally, the magnitude converges when the stress is extremely high ($T \geq 0.8$), as the ruptured area becomes identical in such cases. In the simulations, as already pointed out in AU15, the earthquakes can be divided into two groups: those that have succeeded in progressing to a large event of magnitude 7 or larger and those that arrest soon, thereby leading to a magnitude of about 6 or less. Here we are interested in the former group of larger events.

The results of 13 simulations are summarized in Table 1 and Figure 12 (see also Figure S1 in the supporting information) and also plotted as a function of the stress parameter T in Figure 13. The average residual is small for small T , and it increases with T wherever the hypocenter. The simulations overestimate the ground motions for high T . This is mechanically understandable because a high T facilitates the rupture propagation. In Table 1, we also change the distances used for the residuals to 20–60 km, as it was thought that the ground motions in the near field (< 10 km) and at the regional scale (a few tens of kilometers) could show different tendencies. The residuals and bias become smaller; i.e., the ground motions are closer to the reference GMPE. This is expected, as the used fault models do not have any smaller-scale heterogeneities. In fact, a smooth rupture model is likely to exaggerate the rupture directivity and tends to generate extreme ground motions coherently. On the other hand, when small-scale inhomogeneities are considered on a fault, high slip rate may still exist but do not contribute to the ground motions coherently, avoiding this extreme ground-motion problem. In addition, the fact that the receivers near the source are all located on the sedimentary ocean bottom, while the receivers at distance are on

Table 1. Results From the 13 Simulations Characterized by a Moment Magnitude Greater Than 6.8^a

Model	Regression (1–60 km): See Also Figures 12 and 13				Regression (20–60 km)			
	μ	σ	LLH	p	μ	σ	LLH	p
$T = 0.64$ H1	0.568	0.904	2.148	0.161	0.492	0.880	2.059	0.154
$T = 0.66$ H1	0.846	1.062	2.655	0.113	0.762	1.044	2.530	0.111
$T = 0.68$ H1	1.170	1.154	3.273	0.074	1.092	1.137	3.117	0.074
$T = 0.68$ H2	1.211	1.134	3.312	0.072	1.114	1.036	2.994	0.081
$T = 0.70$ H1	1.206	1.037	3.151	0.080	1.136	1.035	3.029	0.079
$T = 0.70$ H2	1.485	1.199	3.846	0.050	1.335	1.098	3.480	0.058
$T = 0.75$ H1	1.533	0.911	3.618	0.058	1.451	0.918	3.451	0.059
$T = 0.75$ H2	1.795	1.185	4.665	0.028	1.688	1.093	4.243	0.034
$T = 0.78$ H3	0.166	0.784	1.789	0.207	0.089	0.742	1.729	0.194
$T = 0.80$ H3	0.805	1.251	2.921	0.094	0.805	1.216	2.860	0.088
$T = 0.97$ H1	1.945	0.892	4.627	0.029	1.873	0.854	4.381	0.031
$T = 0.97$ H2	2.322	1.216	6.281	0.009	2.209	1.147	5.796	0.012
$T = 0.97$ H3	1.815	1.292	4.906	0.024	1.723	1.266	4.623	0.026

^aThe regressions (mean residual μ and standard deviation σ) with respect to GMPE of *Bindi et al.* [2014] are calculated for distances between 1 and 60 km and between 20 and 60 km, respectively. The former is also shown in Figure 12. Negative average sample log likelihood (LLH) and the revised probability p are calculated from equations (4) and (5), respectively. The model is represented by different T and hypocenters (H1, H2, and H3 correspond to longitude 28.5°E (center), 28.2°E (east), and 28.8°E (west)).

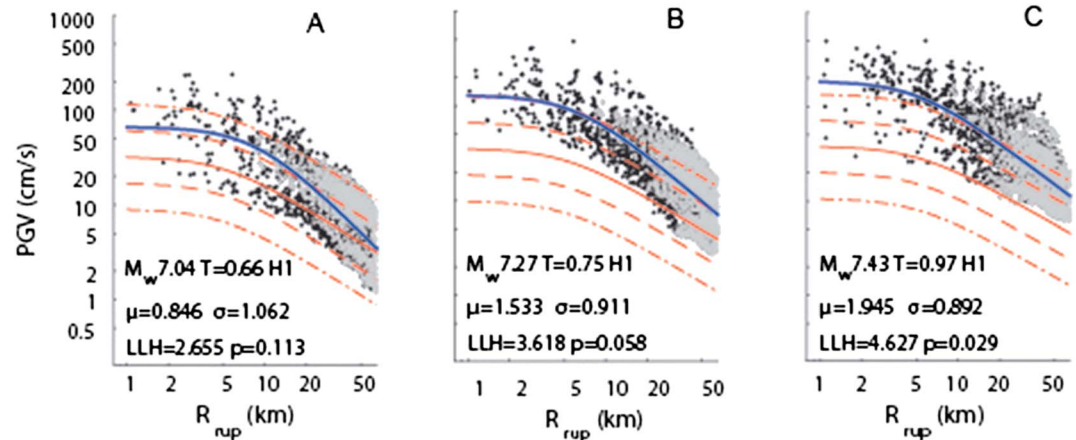


Figure 12. Comparison of the selected three scenarios (shown in Figure 4) of simulated ground motions in terms of PGV with the prediction from the GMPE by *Bindi et al.* [2014] (red line). The simulated values are illustrated as points, among which the gray represents the receivers of $V_s = 1780$ m/s (1-D structure), located on land, far from the source area. The dashed and dash-dotted lines show the median PGV ± 1 and 2 standard deviations of the GMPE. The calculated mean normalized residual (μ), normalized standard deviation (σ), LLH value, and the revised weight (p) are shown in each plot and summarized in Table 1. The blue lines are the regressions for an equation: $PGV = a + b \ln(\sqrt{r^2 + h^2})$, where a , b , and h are the constants and r is the source-receiver distance. This logarithm relation is typically used in GMPE for modeling the decay of ground motion with distance. Thus, the blue line allows comparing the distance decay of the simulated data with the plotted GMPE. All the comparisons of 13 scenarios are shown in Figure S1 in the supporting information.

land where the rock from the assumed 1-D structure ($V_s = 1780$ m/s) is harder, although all are regarded as hard rock sites in the GMPEs, may explain the smaller residual in the far field. However, we still obtain similar results for the revised probability p . This confirms that the formulation based on equations (4) and (5) reattributes the probabilities among the bins appropriately. We recall the hypothesis given in AU15, assigning three levels of the stress parameter T (0.66, 0.75, and 0.97), with associated probabilities of 50% ($T = 0.66$), 35% ($T = 0.75$), and 15% ($T = 0.97$), independently of the other model parameters. To evaluate the revised probabilities, we simply summarize them for three bands: $0.6 < T \leq 0.7$, $0.7 < T \leq 0.8$, and $T > 0.8$, which are shown as a gray surface in Figure 13c. Indeed, this revision is consistent with AU15's hypothesis. The probability of low T is slightly higher (55.0%) than its estimate in AU15, and consequently, extremely high T is less probable (6.2%).

We also compare the SAs at two different periods (1 and 2 s) at the available KOERI station locations (but where there are no data) in Figure 14. *Bindi et al.* [2014] provide the coefficients for the prediction of SAs up to 3 s. Results for three different values of T are compared. The tendency that the residuals are smaller for small T is the same as we observe in the comparison of PGV, so that we can quantify them in the same way. The choice of the PGV as a metric is sufficient to quantify the impact of stress parameter T on the ground motions and to adjust its probability in the logic tree. Nevertheless, the models might not be the best with respect to the GMPE. Some stations with large residuals are strongly affected by the given 3-D structure through which the seismic waves propagate. As discussed in the previous section for the moderate earthquakes, it would be necessary to improve further the 3-D structure and/or take into account a more detailed local structure. The simulations might be biased due to any model parameters and assumption explicitly or implicitly existing in the given logic tree. We discuss this further in the following section.

This revision not only validates the framework of probabilistic seismic hazard assessment previously carried out but also infers the possible crustal strengths. The fault system might be ruptured by low T without waiting for the extremely high accumulation of stress. According to our results, the stress level at which could operate a reasonable $M_w 7+$ earthquake is likely (with a probability of more than 50%) to be in the range of T between 0.6 and 0.7, as previously indicated in Figures 3 and 4. This roughly corresponds to S between 0.67 and 0.43 on an ideally oriented fault (36.65° inclined from the σ_1 axis). This insight needs to be scrutinized from different points of view of current tectonic movement and seismic activity along the North Anatolian Fault.

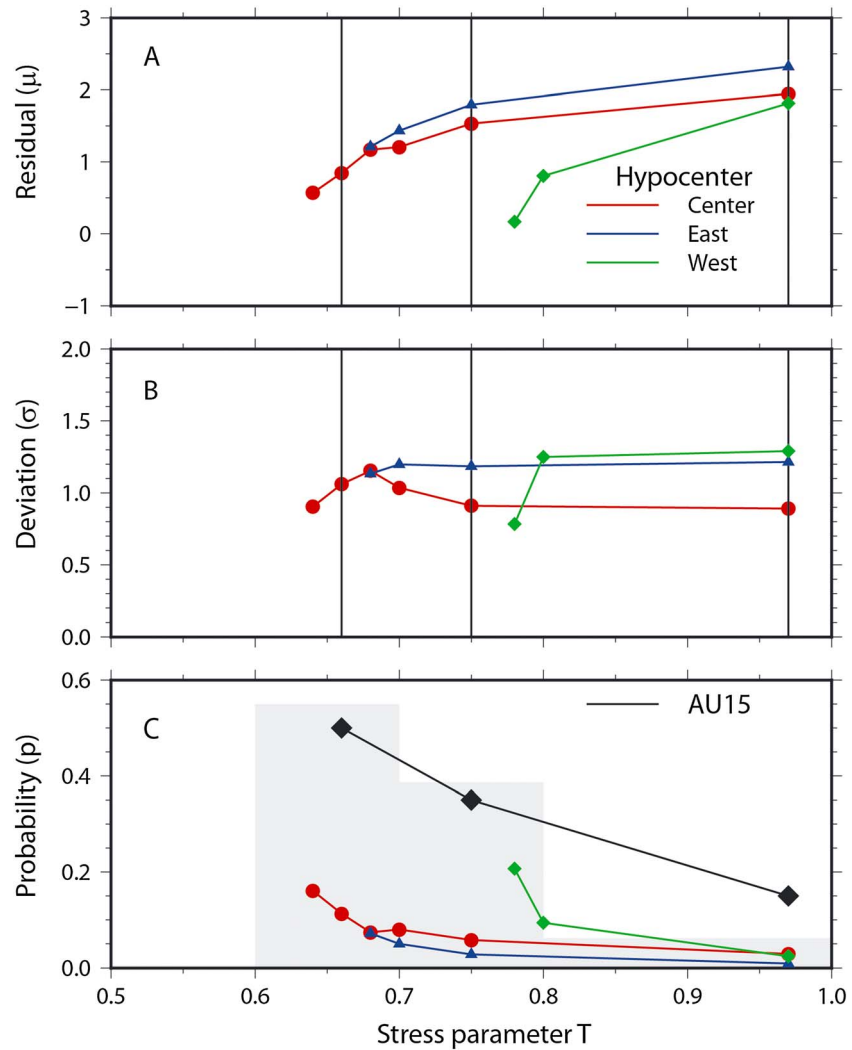


Figure 13. (a) Mean-normalized residual between the simulated PGVs and the prediction from the GMPE [Bindi *et al.*, 2014] for each scenario as function of different hypocenter positions and stress parameter T . (b) The calculated normalized σ from Figure 11. The vertical lines show the three levels of T used in AU15. (c) The revised probability of each scenario by lines and the averaged probability for three levels by gray shadow. For reference, a black line represents the initial probability assumed in the logic tree of AU15.

4. Discussion

We have revised the hypothesis on the stress level based on the expected ground motions with respect to GMPEs. Although the different stress conditions are clear in terms of parameter T from the mechanical point of view, it would still be a challenge to estimate the probability of a given state of regional stress from observations. Thus, we have briefly carried out a statistical analysis on T with a rough resolution width of 0.1. However, the simulations show that the results are sensitive to a small increase of T . Furthermore, we find that the values of T and the hypocenter locations may not be independent. The simulations starting from the central or eastern hypocenters are presented by low T ($0.6 < T \leq 0.7$), while western hypocenters are common for high T ($0.7 < T \leq 0.8$). In other words, within a seismic cycle, a large event will start most probably from the central or eastern parts. However, if the recurrence time was longer (higher T) due to reasons ignored in this study, a large event nucleating from the western hypocenter would become more likely. This is the feature also inferred from AU15 in the given probabilistic framework, but the current study confirms it statistically. This finding is important for further seismic hazard studies in this region and should be carefully considered in future studies [Spagnuolo *et al.*, 2016].

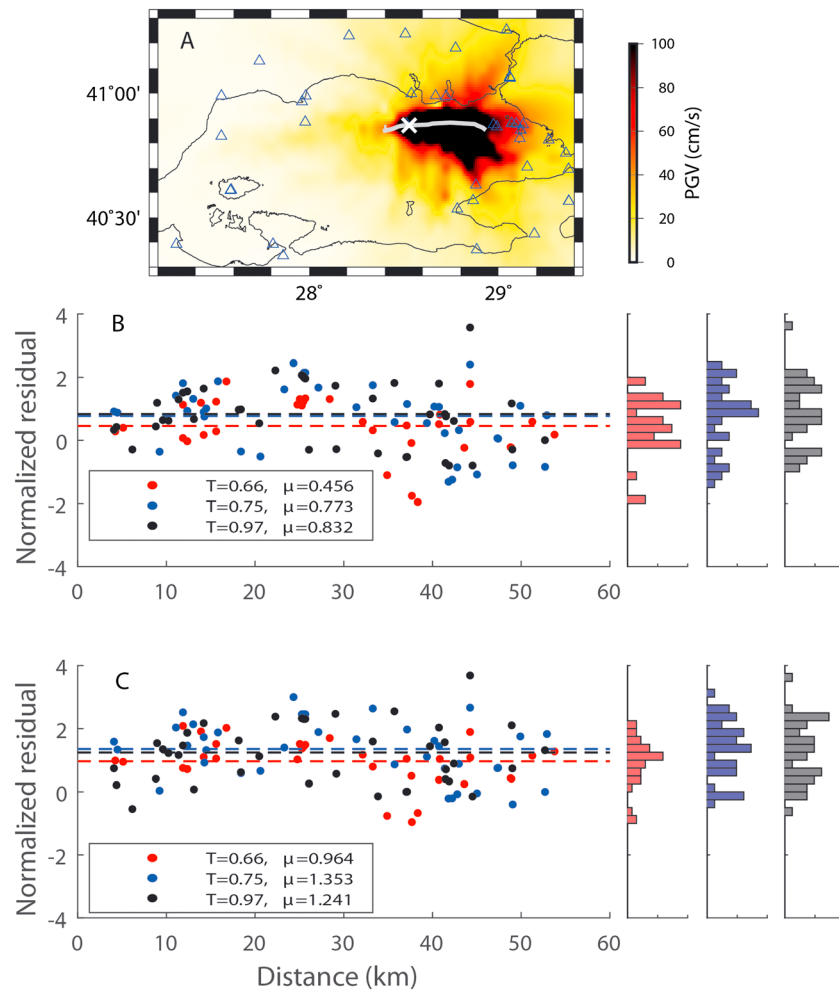


Figure 14. (a) Ruptured fault position and PGV map for a scenario with $T=0.66$ and central hypocenter position (cross mark). Receiver positions used for the calculation of SA are shown by triangles. (b) Residuals for SA (1 s) between the simulations and the GMPE of *Bindi et al.* [2014] are shown for the three scenarios of $T=0.66$ (Figure 14a), 0.75, and 0.97 featuring the same hypocenter location. The horizontal axis represents a distance between the rupture fault and receiver. (c) Residuals for SA (2 s). Also shown on the right-hand side are the histograms of the residuals for the different values of T .

In the formulation of equations (4) and (5) [Scherbaum et al., 2009], the probability is revised relatively among the available bins as a function of LLH. Even if none of the bins are suitable (=a zero residual to a given reference), the probability is assigned accordingly such that the bins of smaller LLH are considered more probable and the summation of the revised probabilities of all bins is equal to unity. Therefore, the probability shown in Figure 13 can be interpreted by the tendency of the ground motions to be stronger for larger T . The dynamic rupture scenarios and 3-D geological structure used in this study might not yet be close enough to reality. On the other hand, the model settings for the rupture scenarios may be biased somehow from the fact that they are positioned as part of a logic tree, and there may be other factors that are not explicitly modeled. For example, earthquake source process could be more complex than the simulations presented here due to small-scale inhomogeneity (e.g., *Mikumo and Miyatake* [1978], *Day* [1982], *Aochi et al.* [2003], *Ripperger et al.* [2008], *Schmedes et al.* [2010], *Shi and Day* [2013], *Mai and Thingbaijam* [2014], and many other studies). Such aspects are important for reproducing and generating ground motions over a large band of frequencies required for engineering applications [e.g., *Mai et al.*, 2010; *Graves and Pitarka*, 2010; *Song et al.*, 2013; *Goulet et al.*, 2015]. *Akinci et al.* [2016] also propose a hybrid ground-motion simulation method combining nonplanar dynamic rupture simulations (AU15), kinematic fractal sum of asperities [Ruiz et al., 2011], and stochastic Green's functions based on a finite source [Boore, 2009]. The relatively smooth slip models might have led to large ground motions in all cases, as the calculated residuals (and consequently σ) are quite large in this

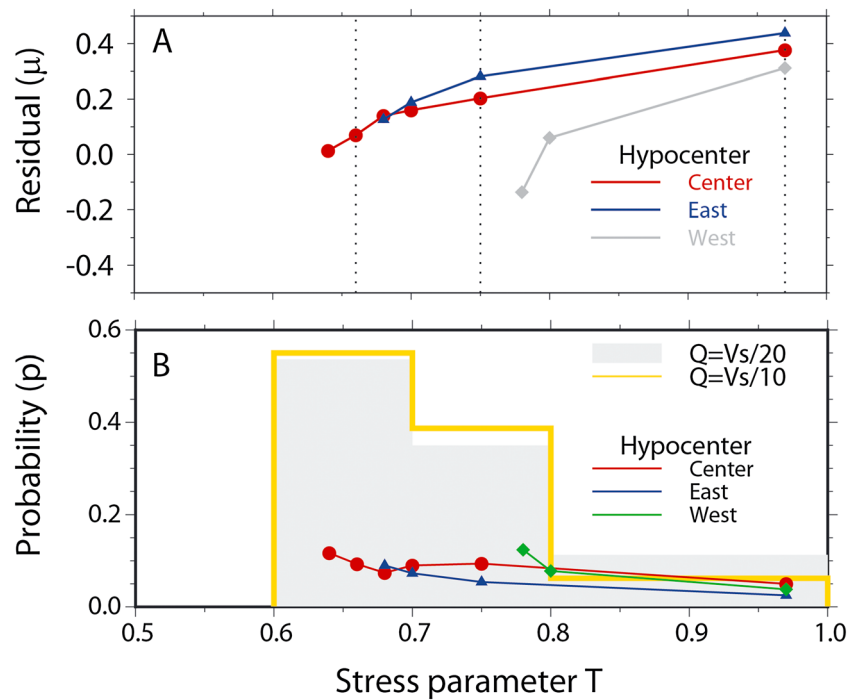


Figure 15. (a) Mean-normalized residual between the simulated PGVs and the prediction from the GMPE [Bindi et al., 2014]. The residual is defined as $\varepsilon = \log_{10}(Y_{GMPE}) - \log_{10}(Y_{simulation})$ for ground-motion parameter y . The simulations are carried out assuming $Q = V_s/20$. Although this assumption give worse GoF than the assumption $Q = V_s/10$ when considering the two moderate earthquakes of Figure 6, the normalized residual are lower. (b) The revised probability of each scenario is shown by the red, blue, and green lines. The averaged probability for three stress levels is displayed as a gray shadow. For reference, the orange line shows the probability obtained in Figure 13 for the case of $Q = V_s/10$. Despite the bias introduced by the assumption $Q = V_s/20$, the obtained probabilities are relatively similar.

study, because of ignored factors such as fault heterogeneity (see above) or off-plane damaging [e.g., Andrews, 2005; Roten et al., 2014]. Yet our discussion is still valid. Although the presented simulations are still limited (with only a single variable T), this is the simplest way to evaluate the probability of the given model parameters by fixing all the other parameters. The process adopted in this study can be useful when scrutinizing dynamically simulated earthquake scenarios and to assign them a priority to communicate to engineers which scenarios are the most probable.

As a simple example of model bias, let us carry out ground-motion simulations assuming $Q = V_s/20$, although this was not better in our tests for the two moderate earthquakes than assuming a constant Q or $Q = V_s/10$. Under such a strong attenuation condition, the wave propagation is significantly changed and the simulated PGVs get closer to the GMPE, i.e., smaller residuals, for the same earthquake scenarios (Figure 15). This changes the values of LLH, and the probabilities are revised accordingly. Nevertheless, the revised probabilities are relative among the bins, and the tendency of the role of stress parameter T on the ground motions is similar. This leads to the same conclusion that lower levels of T are preferred and an extreme level of high T is less probable, supporting the hypothesis taken in AU15.

5. Summary

We have carried out ground-motion simulations in the Marmara Sea (Turkey) region using a 3-D finite difference method taking into account the 3-D geological structure of this region. First, two moderate earthquakes of about magnitude 5 have been simulated and the goodness of fit of the simulated ground-motion parameters to the observations have been evaluated. The 3-D structure assuming a quality factor $Q = V_s/10$ led to a better match among our tests.

Second, we have attempted to constrain the regional stress levels that allow a future large earthquake of magnitude of about 7 or larger, focusing on the stress parameter T . Several hypotheses for this mechanical

parameter and their associated likelihoods were introduced by a logic tree approach in Aochi and Ulrich [2015] to estimate the likelihood of the earthquake scenarios. We have proposed a strategy for reevaluating these hypotheses by making use of published ground motion prediction equations (GMPEs) for engineering strong motion parameters. The simulations being valid up to frequencies of about 1 Hz, we were able to compare the simulated horizontal peak ground velocity (PGV) with the PGVs predicted by various GMPEs. It was shown that high-stress conditions (high T) leads to large earthquakes as well as high resulting ground motions. By quantifying the overall difference between simulated PGV and estimates from GMPEs, we were able to estimate the probability of each scenario. Namely, a high absolute residual means a less probable scenario. Finally, we are able to revise the probability of the stress field in terms of T . A moderate T ($0.6 < T \leq 0.7$) has a probability of more than 50%, and an extremely high T (> 0.8) is unlikely (probability less than 10%). These results are coherent with our previous hypotheses based on expert judgment. This constraint from comparisons with GMPEs is important not only for further quantitative seismic hazard assessments and for investigating the likelihood of probable and extremes of dynamic rupture scenarios for ground-motion estimations but also to understand dynamic rupture processes along nonplanar fault systems and the crustal strength in geodynamic processes. The same model parameterization could be used for other earthquake scenarios of analogous fault geometric complexity and the fault maturity as in this part of the North Anatolian Fault.

Acknowledgments

This work has predominantly been undertaken in the framework of the European Commission's Seventh Programme under the project MARSite (308417) during the period of 2012–2016. We thank Krabulut, Bayrakci, and other colleagues from the MARSite project for their fruitful discussions and their published/unpublished information. The ground-motion data are available from <http://www.koeri.boun.edu.tr/sismo/indexeng.htm>. Numerical simulations were carried out at the French national supercomputing center, Grand Equipement National de Calcul Intensif (CINES), under grant 46700. Finally, we thank Martin Mai and two anonymous reviewers for their careful and detailed comments on an earlier version of this study.

References

- Akinci, A., H. Aochi, A. Herrero, M. Pischuita and D. Karanikas (2016), Physics-based broadband ground motion simulations for probable $M > 7.0$ earthquakes in the Marmara Sea region (Turkey), *Bull. Seismol. Soc. Am.*, in press.
- Akkar, S., M. A. Sandikkaya, and J. J. Bommer (2014a), Empirical ground-motion models for point- and extended-source crustal earthquake scenarios in Europe and the Middle East, *Bull. Earthquake Eng.*, *12*(1), 359–387, doi:10.1007/s10518-013-9461-4.
- Akkar, S., M. A. Sandikkaya, and J. J. Bommer (2014b), Erratum to: Empirical ground-motion models for point- and extended-source crustal earthquake scenarios in Europe and the Middle East, *Bull. Earthquake Eng.*, *12*(1), 389–390, doi:10.1007/s10518-013-9508-6.
- Andrews, D. J. (2005), Rupture dynamics with energy loss outside the slip zone, *J. Geophys. Res.*, *110*, B101307, doi:10.1029/2004JB003191.
- Aochi, H., and J. Douglas (2006), Testing the validity of simulated strong ground motion from the dynamic rupture of a fault system, by using empirical equations, *Bull. Earthquake Eng.*, *4*, 211–229.
- Aochi, H., and M. Yoshimi (2016), Seismological asperities from the point of view of dynamic rupture modelling: The 2007 M_w 6.6 Chuetsu-Oki, Japan, earthquake, *J. Seismol.*, *20*, 1089–1105, doi:10.1007/s10950-016-9569-5.
- Aochi, H., and R. Madariaga (2003), The 1999 Izmit, Turkey, earthquake: Non-planar fault structure, dynamic rupture process and strong ground motion, *Bull. Seismol. Soc. Am.*, *93*, 1249–1266, doi:10.1785/0120020167.
- Aochi, H., and T. Ulrich (2015), A probable earthquake scenario near Istanbul determined from dynamic simulations, *Bull. Seismol. Soc. Am.*, *105*, 1468–1475, doi:10.1785/0120140283.
- Aochi, H., E. Fukuyama and R. Madariaga (2003), Constraints of fault constitutive parameters inferred from non-planar fault modeling, *Geochem. Geophys. Geosyst.*, *4*(2), 1020, doi:10.1029/2001GC00207.
- Aochi, H., V. Durand, and J. Douglas (2011), Influence of super-shear earthquake rupture models on simulated near-source ground motion from the 1999 Izmit (Turkey) earthquake, *Bull. Seismol. Soc. Am.*, *101*, 726–741, doi:10.1785/0120100170.
- Aochi, H., T. Ulrich, A. Duceillier, F. Dupros, and D. Michea (2013), Finite difference simulations of seismic wave propagation for understanding earthquake physics and predicting ground motions: Advances and challenges, *J. Phys. Conf. Ser.*, *454*, 012010, doi:10.1088/1742-6596/1/012010.
- Atakan, K., A. Ojeda, M. Meghaoui, A. A. Barka, M. Erdik, and A. Bodare (2002), Seismic hazard in Istanbul following the 17 August 1999 Izmit and 12 November 1999 Düzce earthquakes, *Bull. Seismol. Soc. Am.*, *92*, 446–482.
- Baumann, C., and L. A. Dalguer (2014), Evaluating the compatibility of dynamic rupture-based synthetic ground motion with empirical ground-motion prediction equation, *Bull. Seismol. Soc. Am.*, *104*, 634–652, doi:10.1785/0120130077.
- Bayrakci, G., M. Lige, A. Bécel, A. Hirn, T. Taymaz, S. Yolsal-Çevikbilen, and SEISMARMARA team (2013), 3-D sediment-basement tomography of the Northern Marmara trough by a dense OBS network at the nodes of a grid of controlled source profiles along the North Anatolian Fault, *Geophys. J. Int.*, *194*, 1335–1357, doi:10.1093/gji/ggt211.
- Bindi, D., M. Massa, L. Luzi, G. Ameri, F. Pacor, R. Puglia, and P. Augliera (2014), Pan-European ground-motion prediction equations for the average horizontal component of PGA, PGV, and 5%-damped PSA at spectral periods up to 3.0 s using the RESORCE dataset, *Bull. Earthquake Eng.*, *12*(1), 391–430, doi:10.1007/s10518-013-9525-5.
- Boore, D. M. (2009), Comparing stochastic point-source and finite-source ground-motion simulations: SMSIM and EXSIM, *Bull. Seismol. Soc. Am.*, *99*, doi:10.1785/0120090056.
- Boore, D. M., J. P. Stewart, E. Seyhan, and G. M. Atkinson (2014), NGA-West 2 equations for predicting PGA, PGV, and 5%-damped PSA for shallow crustal earthquakes, *Earthquake Spectra*, *30*(3), 1057–1085, doi:10.1193/070113EQS184M.
- Bouchon, M., M. N. Toksöz, H. Karabulut, M.-P. Bouin, M. Dietrich, M. Aktar, and M. Edie (2002), Space and time evolution of rupture and faulting during the 1999 Izmit (Turkey) earthquake, *Bull. Seismol. Soc. Am.*, *92*, 256–266.
- Cauzzi, C., E. Faccioli, M. Vanini, and A. Bianchini (2015), Updated predictive equations for broadband (0.01–10 s) horizontal response spectra and peak ground motions, based on a global dataset of digital acceleration records, *Bull. Earthquake Eng.*, *13*(6), 1587–1612, doi:10.1007/s10518-014-9685-y.
- Das, S., and K. Aki (1977), A numerical study of two-dimensional spontaneous rupture propagation, *Geophys. J. R. Astron. Soc.*, *50*, 643–668.
- Day, S. M. (1982), Three-dimensional simulation of spontaneous rupture: The effect of non-uniform prestress, *Bull. Seismol. Soc. Am.*, *72*, 1881–1902.
- Day, S. M., and C. R. Bradley (2001), Memory-efficient simulation of anelastic wave propagation, *Bull. Seismol. Soc. Am.*, *91*, 520–531.

- Delavaud, E., F. Scherbaum, N. Kuehn, and T. Allen (2012), Testing the global applicability of ground-motion prediction equations for active shallow crustal regions, *Bull. Seismol. Soc. Am.*, *02*, 707–721, doi:10.1785/0120110113.
- Douglas, J. (2003), Earthquake ground motion estimation using strong-motion records: A review of equations for the estimation of peak ground acceleration and response spectral ordinates, *Earth Sci. Rev.*, *61*(1–2), 43–104.
- Douglas, J., and H. Aochi (2016), Assessing components of ground-motion variability from simulations for the Marmara Sea region (Turkey), *Bull. Seismol. Soc. Am.*, *106*(1), 300–306, doi:10.1785/0120150177.
- Douglas, J., T. Ulrich, D. Bertil, and J. Rey (2014), Comparison of the ranges of uncertainty captured in different seismic-hazard studies, *Seismol. Res. Lett.*, *85*(5), 977–985, doi:10.1785/0220140084.
- Erdik, M., M. Demircioğlu, K. Sesetyan, E. Durukal, and B. Siyahi (2004), Earthquake hazard in Marmara region, Turkey, *Soil Dyn. Earthquake Eng.*, *24*, 605–631.
- Ergintav, S., R. E. Reilinger, R. Çakmak, M. Floyd, Z. Cakir, U. Doğan, R. W. King, S. McClusky, and H. Özener (2014), Istanbul's earthquake hot spots: Geodetic constraints on strain accumulation along faults in the Marmara seismic gap, *Geophys. Res. Lett.*, *41*, 5783–5788, doi:10.1002/2014GL060985.
- Goulet, C. A., N. A. Abrahamson, P. G. Somerville, and K. E. Woodell (2015), The SCEC broadband platform validation exercise for pseudo-spectral acceleration: Methodology for code validation in the context of seismic hazard analyses, *Seismol. Res. Lett.*, *86*, doi:10.1785/0220140101.
- Graves, R. (1996), Simulating seismic wave propagation in 3D elastic media using staggered-grid finite differences, *Bull. Seismol. Soc. Am.*, *86*, 1091–1106.
- Graves, R., and A. Pitarka (2010), Broadband ground-motion simulation using a hybrid approach, *Bull. Seismol. Soc. Am.*, *100*, 2095–2123, doi:10.1785/0120100057.
- Harris, R. A., J. F. Dolan, R. Hartleb, and S. M. Day (2002), The 1999 Izmit, Turkey earthquake: A 3D dynamic stress transfer model of intraearthquake triggering, *Bull. Seismol. Soc. Am.*, *92*, 245–255, doi:10.1785/0120000825.
- Horikawa, H., et al. (2008), A three-dimensional subsurface structure model of the Chukyo area, central Japan, National Institute of Advanced Industrial Science and Technology (AIST)–Geological Survey of Japan, *Annu. Rep. Active Fault Paleoseismicity Res.*, *8*, 203–254.
- Kristek, J., and P. Moczo (2003), Seismic-wave propagation in viscoelastic media with material discontinuities: A 3D fourth-order staggered-grid finite-difference modeling, *Bull. Seismol. Soc. Am.*, *93*, 2273–2280.
- Le Pichon, X., N. Chamot-Rooke, C. Rangin and A. M. C. Sengör (2003), The North Anatolian Fault in the Sea of Marmara, *J. Geophys. Res.*, *108*(B4), 2179, doi:10.1029/2002JB001862.
- Ludwig, W. J., J. E. Nafe, and C. L. Drake (1970), Seismic refraction, in *The Sea: Ideas and Observations on Progress in the Study of the Seas*, vol. 4, edited by A. E. Maxwell, pp. 53–84, Wiley, New York.
- Mai, P. M., and K. K. S. Thingbaijam (2014), SRCMOD: An online database of finite-fault rupture model, *Seismol. Res. Lett.*, *85*, 1348–1357, doi:10.1785/0220140077.
- Mai, P. M., W. Imperatori, and K. B. Olsen (2010), Hybrid broadband ground-motion simulations: Combining long-period deterministic synthetics with high-frequency multiple S-to-S backscattering, *Bull. Seismol. Soc. Am.*, *100*, 2124–2142, doi:10.1785/0120080194.
- McGarr, A. (1999), On relating apparent stress to the stress causing earthquake fault slip, *J. Geophys. Res.*, *104*, 3003–3011, doi:10.1029/1998JB900083.
- Mikumo, T., and T. Miyatake (1978), Dynamic rupture process on a three-dimensional fault with non-uniform friction and near field seismic waves, *Geophys. J. R. Astron. Soc.*, *54*, 417–438.
- Oglesby, D. D., and P. M. Mai (2012), Fault geometry, rupture dynamics and ground motion from potential earthquakes on the North Anatolian Fault under the Sea of Marmara, *Geophys. J. Int.*, *188*, 1071–1087.
- Oglesby, D. D., P. M. Mai, K. Atakan, and S. Pucci (2008), Dynamic models of earthquakes on the North Anatolian Fault zone under the Sea of Marmara: Effect of hypocenter location, *Geophys. Res. Lett.*, *35*, L18302, doi:10.1029/2008GL035037.
- Olsen, K. B., and J. E. Mayhew (2010), Goodness-of-fit criteria for broadband synthetic seismograms, with application to the 2008 Mw5.4 Chino Hills, CA, earthquake, *Seismol. Res. Lett.*, *81*, 715–723.
- Parsons, T. (2004), Recalculated probability of $M \geq 7$ earthquakes beneath the Sea of Marmara, Turkey, *J. Geophys. Res.*, *109*, B05304, doi:10.1029/2003JB002667.
- Pulido, N., A. Ojeda, K. Atakan, and T. Kubo (2004), Strong ground motion estimation in the Sea of Marmara region (Turkey) based on a scenario earthquake, *Tectonophysics*, *391*, 357–374.
- Ripperger, J., P. M. Mai, and J.-P. Ampuero (2008), Variability of near-field ground motion from dynamic earthquake rupture simulations, *Bull. Seismol. Soc. Am.*, *98*, 1207–1228, doi:10.1785/0120070076.
- Roten, D., K. B. Olsen, S. M. Day, Y. Cui, and D. Fah (2014), Expected seismic shaking in Los Angeles reduced by San Andreas Fault zone plasticity, *Geophys. Res. Lett.*, *41*, 2769–2777, doi:10.1002/2014GL059411.
- Ruiz, J. A., D. Baumont, P. Bernard, and C. Berge-Thierry (2011), Modelling directivity of strong ground motion with a fractal, k^{-2} kinematic source model, *Geophys. J. Int.*, *186*, 22,644, doi:10.1111/j.1365246X.2011.05000.x.
- Scherbaum, F., E. Delavaud, and C. Riggelsen (2009), Model selection in seismic hazard analysis: An information-theoretic perspective, *Bull. Seismol. Soc. Am.*, *99*, 3234–3247, doi:10.1785/0120080347.
- Schmedes, J., R. J. Archuleta, and D. Lavallee (2010), Correlation of earthquake source parameters inferred from dynamic rupture simulations, *J. Geophys. Res.*, *115*, B03304, doi:10.1029/2009JB006689.
- Shi, Z., and S. M. Day (2013), Rupture dynamics and ground motion from 3-D rough-fault simulations, *J. Geophys. Res. Solid Earth*, *118*, 1122–1141, doi:10.1002/jgrb.50094.
- Song, S. G., L. A. Dalguer, and P. M. Mai (2013), Pseudo-dynamic source modelling with 1-point and 2-point statistics of earthquake source parameters, *Geophys. J. Int.*, *196*, 1770–1786, doi:10.1093/gji/ggt479.
- Spagnuolo, E., A. Akinci, A. Herrero, and S. Pucci (2016), Implementing the effect of the rupture directivity on PSHA for the city of Istanbul, Turkey, *Bull. Seismol. Soc. Am.*, *106*, doi:10.1785/0120160020.